Poleward shift of subtropical highs drives Patagonian glacier mass loss

Brice Noël*[1], Stef Lhermitte[2,3], Bert Wouters[3], Xavier Fettweis[1]

[1] *Laboratoire de Climatologie et Topoclimatologie, University of Liège, Liège, Belgium.*
[2] *Department of Earth & Environmental Sciences, KU Leuven, Leuven, Belgium.*
[3] *Department of Geoscience & Remote Sensing, Delft University of Technology, Delft, Netherlands.*

Patagonian glaciers have been rapidly losing mass in the last two decades, but driving processes remain poorly known. Here we use two state-of-the-art regional climate models to reconstruct longterm (1940-2023) glacier surface mass balance (SMB), i.e., the difference between precipitation accumulation and surface runoff, at about 5 km spatial resolution, further statistically downscaled to a 500 m grid. High-resolution SMB agrees well with in-situ observations and, combined with solid ice discharge estimates, reconciles recent GRACE/GRACE-FO satellite mass change. Glacier mass loss coincides with a longterm SMB decline (-0.42 Gt yr^{-2}), primarily driven by enhanced surface runoff (+0.58 Gt yr^{-2}) and steady precipitation. We link these trends to a poleward shift of the subtropical highs favouring warm northwesterly air advections towards Patagonia (+0.14°C dec^{-1} at 850 hPa). Since the 1940s, Patagonian glaciers have lost 1,471 $\pm$ 202 Gt of ice, equivalent to a 4.1 $\pm$ 0.6 mm global mean sea-level rise.

Introduction

Situated in the Southern Andes, Patagonia hosts the largest glacier area within the southern hemisphere, excluding the Antarctic ice sheet[1–3]. Besides small mountain glaciers, Patagonia encompasses three major icefields, namely the Northern (NPI; 4,000 km^2)[4] and Southern Patagonian Icefields (SPI; 13,000 km^2)[5], and the Cordillera Darwin Icefield (CDI; 2,600 km^2)[6] located in the Tierra del Fuego archipelago (inset maps in Fig. 1a). Patagonian glaciers are on average 181 m thick[2], with a maximum of 1,400 m in deep glacial valleys[3]. Altogether, these glaciers hold 5,350 km^3 to 5,500 km^3 of ice[2,7,8], eventually raising global sea level by $\sim$13 mm if totally melted. Extrapolation of glaciological and geodetic observations suggests that Patagonia has experienced glacier mass loss since the early 1960s, contributing about 3.3 mm to global sea-level rise in the period 1961-2016[7]. Recent remote sensing studies spanning the last two decades have reported rapid glacier mass loss ranging from 19 to 22 Gt yr^{-1} in the period 2000-2019[9–11], equivalent to an average 0.06 mm sea-level rise each year. The three major icefields are responsible for 83% of this mass loss[9], while the remainder is attributed to smaller neighbouring mountain glaciers. Storing only 3% of the Earth's total ice volume outside polar ice sheets[2], Patagonia is disproportionately responsible for $\sim$10% of the glacier

1

contribution to sea-level rise (2002-2016)[12].

Mass change (MB) of Patagonian glaciers can be quantified by subtracting solid ice discharge (D), i.e., frontal ablation of calving icebergs, from the glacier surface mass balance (SMB), i.e., the difference between mass gained from precipitation, and lost from meltwater runoff and sublimation. NPI and SPI icefields generally discharge ice into the ocean on the western side of the Andes, while they typically flow into proglacial lakes on the eastern side[1]. Remotely sensed D estimates indicate that NPI and SPI accounted for 15.1 ± 1.1 Gt yr^{-1} on average in 1968-1999[1],which further increased to 24.1 ± 1.7 Gt yr^{-1} in 2000-2019[13]. SPI floating glaciers contributed about 80% to the total D flux in 1968-1999[1], and up to 90% in 2000-2019[13]. Since the 2000s, SPI ice discharge has however undergone a decreasing trend[13]. This reveals that glacier SMB decline has been playing an increasing role in the recent Patagonian glacier mass loss[14], which is expected to further accelerate in the future[15,16]. In contrast, SMB reconstructions in NPI and SPI using positive degree day (PDD)[17], regional climate models[18], sometimes statistically downscaled[14,19,20], suggest a positive but insignificant SMB trend in the period 1975-2015. This trend was ascribed to longterm snowfall increase combined with meltwater runoff decline. However, these results remain highly uncertain since low-resolution climate models are prone to overestimate precipitation over the steep Andes[21], while they cannot accurately capture high meltwater runoff rates across narrow glaciers[18]. Furthermore, a positive SMB trend contradicts the recent mass loss increase observed in the last two decades[9–11,22–24], highlighting large uncertainties in modelled SMB and a poor understanding of mass change drivers.

Here we use two state-of-the-art regional climate models, namely MAR version 3.14 (1940-2023) and RACMO version 2.3p2 (1979-2023)[18,25], to reconstruct the contemporary SMB of Patagonian glaciers at 5 km and 5.5 km spatial resolution respectively (Supplementary Fig. 1) (Methods). Both models are forced by the latest ERA5 climate reanalysis[26] and statistically downscaled to a 500 m grid[27,28] (Methods). In brief, statistical downscaling uses daily, local vertical gradients to correct SMB and components, i.e., total precipitation, snowfall, total sublimation, total melt and subsequent runoff, for elevation difference between the low-resolution surface topography prescribed in both models, and the high-resolution Shuttle Radar Topography Mission (SRTM) digital elevation model (DEM)[29] at 30 m resolution, down-sampled to a 500 m grid (Supplementary Fig. 2). Moderate Resolution Imaging Spectroradiometer (MODIS) albedo records at 500 m resolution are further used to correct surface melt and runoff for the albedo of exposed dark bare ice in summer. Adjustments for overestimated surface runoff in MAR (12.5%) and total precipitation in RACMO (32.5%) are then applied to the statistically downscaled SMB products to reconcile remotely sensed mass change from the Gravity Recovery and Climate Experiment (GRACE) and Follow-On (GRACE-FO) missions[24], when combined to solid ice discharge[1,13]. We use our downscaled SMB products to identify the drivers of Patagonian glacier mass loss, and estimate their contribution to global sea-level rise.

Results

Mass change of Patagonian glaciers

Figure 1a shows longterm Patagonian glacier mass change (MB = SMB - D) derived from MAR (green line; 1940-2023) and RACMO SMB (blue line; 1979-2023), further statistically downscaled to 500 m (Fig. 2c and Supplementary Fig. 3c), and from previously published D estimates[1,13]. In 1940-1999[1], D is set to 15.1 ± 1.1 Gt yr^{-1} and increases to 24.1 ± 1.7 Gt yr^{-1} in 2000-2023[13]. Since 1940, Patagonian glaciers have been experiencing sustained mass loss (MB < 0), though briefly interrupted by a short mass gain episode (MB > 0) in the period 1945-1955 (Fig. 1a). This longterm negative trend is in line with geodetic mass change records spanning 1961-2016 (grey dots)[7], with averaged observed and modelled mass loss of 26.2 ± 11.0 Gt yr^{-1} (Geodetic)[7] and 25.1 ± 2.4 Gt yr^{-1} (MAR) respectively. Modelled mass loss from MAR (28.1 ± 2.4 Gt yr^{-1}) and RACMO (29.3 ± 2.4 Gt yr^{-1}) also aligns well with GRACE/GRACE-FO satellite measurements (28.8 ± 11.0 Gt yr^{-1}) (red line) in the last two decades (2002-2022), showing both a strong correlation (R^2 = 0.93) and a low RMSE (∼50 Gt) for both models (Supplementary Fig. 4c). Using our two high-resolution products, we estimate that Patagonian glaciers have lost 1,471 ± 202 Gt of ice since 1940, contributing 4.1 ± 0.6 mm to global mean sea-level rise.

Longterm surface mass balance trends

To explore the role of surface processes in the longterm mass loss, Figure 1b shows annual cumulative SMB and components from both MAR (solid lines; 1940-2023) and RACMO models (bands; 1979-2023), statistically downscaled to 500 m (Fig. 2a-c and Supplementary Fig. 3a-c). For SMB evaluation, we use 74 stake measurements (1980-2019) collected at 38 in situ sites across NPI (2 sites), SPI (26 sites), and CDI (19 sites) (yellow stars in the inset maps of Fig. 1a) (Methods). MAR and RACMO agree well with observations, i.e., R^2 reaches 0.85 and 0.77, and RMSE ranges from 2.3 to 4.1 m water equivalent (w.e.) respectively (Supplementary Fig. 5c,f). Cross-model comparison between each SMB component in the overlapping period 1979-2023 shows good agreement, with high correlation (0.82 ≤ R^2 ≤ 0.93) and overall small model differences (0 to 11%) (Supplementary Fig. 6a-e) (Methods). Although glacier-integrated amounts are almost identical, low correlation is found for modelled retention and refreezing in firn (Supplementary Fig. 6f), i.e., the perennial compressed snow layer covering the glacier accumulation areas (SMB > 0 in the inset maps of Fig. 1a). We attribute these discrepancies to the different snow modules incorporated in MAR and RACMO (Methods). Supplementary Fig. 3d-f shows spatial differences between downscaled SMB components from MAR and RACMO at 500 m. Total precipitation shows large-scale spatial differences between the two models, i.e., with lower values in MAR on the western windside slope, and higher values on the eastern leeside (Supplementary Fig. 3d). This indicates a more pro-

nounced foehn effect on the Patagonian Andes from prevailing westerly winds in RACMO relative to MAR. In fact, RACMO generally overestimates orographic-forced precipitation in this region[18,21]. In addition, MAR has lower runoff than RACMO (2.2 Gt yr^{-1} in Supplementary Fig. 6d and Supplementary Table 1), notably inland the icefields (Supplementary Fig. 3e). This results from higher meltwater refreezing and retention in firn (0.3 Gt yr^{-1} in Supplementary Fig. 6f) combined with lower rainfall in MAR (2.7 Gt yr^{-1} in Supplementary Fig. 6c). Consequently, glacier-integrated SMB is almost equal in both models (0.7 Gt yr^{-1} in Supplementary Fig. 6a), and spatial differences are mostly driven by precipitation distribution patterns (Supplementary Fig. 3f). To ensure reliable surface accumulation, we compare modelled glacier-integrated total precipitation with corresponding estimates from the gridded meteorological PMET data set at 5 km spatial resolution (1980-2020)[30] (Supplementary Fig. 7). We find excellent model agreement (R^2 = 0.87 and 0.90) with low RMSE of 10.6 Gt yr^{-1} and 8.9 Gt yr^{-1}, i.e., equivalent to 4% and 5% of the PMET total precipitation, in MAR and RACMO respectively.

Using longterm MAR timeseries (Fig. 1b), we find that Patagonian glacier SMB (Fig. 2c) remained close to equilibrium at 0.1 ± 0.7 Gt yr^{-1} on average (1940-2023), the result of total precipitation (198.7 ± 1.5 Gt yr^{-1}) (Fig. 2a), i.e., partitioned in snowfall (77%) and rainfall (23%), approximately balancing surface runoff (199.7 ± 2.2 Gt yr^{-1}) (Fig. 2b) (Supplementary Table 1). At the same time, SMB experiences large interannual variability (SD = 31.4 Gt yr^{-1}), primarily driven by runoff fluctuations (SD = 26.1 Gt yr^{-1}) being 45% larger than those of total precipitation (SD = 18.0 Gt yr^{-1}). Large interannual variability is illustrated by peak high and low SMB reaching +70.2 Gt in year 1948, and -66.4 Gt in year 2016 (Fig. 1b). In these years, SMB is three to five-folds larger than the corresponding D flux (15.1 to 24.1 Gt)[1,13], indicating that SMB fluctuations primarily drive the variability and trend of Patagonian glacial mass change. In the period 1940-2023, we find that Patagonian glaciers have undergone sustained, and significant SMB decline (-0.42 ± 0.27 Gt yr^{-2}, p < 0.01) (Fig. 1b). This results from insignificant total precipitation increase (0.15 ± 0.16 Gt yr^{-2}, p > 0.05) notably in the glacier interior accumulation zones (Fig. 2d), combined with significantly enhanced surface runoff (0.58 ± 0.20 Gt yr^{-2}, p < 0.01) across low-lying glacier ablation zones (Fig. 2e). Interestingly, the insignificant precipitation trend stems from steady snowfall accumulation (0.04 ± 0.14 Gt yr^{-2}, p > 0.05) with significant rainfall increase (0.11 ± 0.05 Gt yr^{-2}, p < 0.01). The increase in runoff coincides with a significant rise in glacier near-surface air temperature (T2m) (0.10 ± 0.03^{o}C dec^{-1}, p < 0.01), hence triggering enhanced meltwater (0.56 ± 0.20 Gt yr^{-2}, p < 0.01). Atmospheric warming is in line with two gridded meteorological data sets at 5 km spatial resolution, namely CR2MET (1960-2021)[31] and PMET (1980-2020)[30] (Fig. 1c). We conclude that, following longterm atmospheric warming (1940-2023), enhanced runoff at the glacier margins (Fig. 2e) exceeds the small precipitation increase inland (Fig. 2d), in turn significantly reducing SMB (Fig. 2f).

Drivers of longterm runoff increase

Patagonian glacier SMB strongly correlates with surface runoff in both MAR and RACMO (r = 0.80) (Fig. 3a), while the signal is much weaker for total precipitation (r = 0.57; not shown). This confirms that longterm Patagonian glacier SMB responds predominantly to runoff rather than precipitation changes (Fig. 2d-f). At the same time, runoff is highly sensitive to glacier near-surface temperature anomalies with respect to 1960-1989 (r = 0.81) (Fig. 3b), indicating that longterm atmospheric warming triggers runoff increase. To investigate the link between atmospheric warming and runoff, Figure 4a-c shows longterm ablation zone extent (SMB < 0) as a fraction of the total glacier area; the fraction of total precipitation falling as rain; and the glacier refreezing capacity, i.e., the fraction of rain and meltwater effectively retained or refrozen within the firn layer. The latter three quantities are first correlated to near-surface temperature anomalies (Fig. 4d-f) and then to surface runoff (Fig. 4g-i). MAR and RACMO agree well in the overlapping period 1979-2023, with strong correlation and small model differences for the ablation zone extent (R^2 = 0.89, difference = -1.2%), rainfall fraction (R^2 = 0.92, difference = -0.6%), and firn refreezing capacity (R^2 = 0.84, difference = 0.1%) (Fig. 4a-c).

Using longterm MAR timeseries, we find that the glacier ablation zones have significantly expanded since 1940 (+0.9% dec^{-1}, p < 0.01), following near-surface atmospheric warming (r = 0.75, Fig. 4d). Ablation zone expansion triggers runoff increase (r = 0.85, Fig. 4g) as enhanced melt eventually drains on top of impermeable bare ice exposed at the surface in summer. Furthermore, the contribution of rainfall to total precipitation has significantly increased (+0.4% dec^{-1}, p < 0.01), the result of atmospheric warming favouring precipitation in the liquid phase (r = 0.67, Fig. 4e), which preferentially runs off on top of bare ice surfaces (r = 0.83, Fig. 4h). In the interior accumulation zone, firn retains roughly 25% of surface melt and rain in its pore space on average (1940-2023). Since 1940, firn refreezing capacity has significantly declined (-0.3% dec^{-1}, p < 0.01) (Fig. 4c) following atmospheric warming (r = 0.71, Fig. 4f). This results in increased surface runoff across the glacier interior accumulation zone (r = 0.89, Fig. 4i) through i) the progressive removal of the firn layer, ii) a reduced firn replenishment as rainfall increases at the expense of snowfall, and iii) the depletion of available firn pore space following enhanced surface melt and rain storage. Through these combined processes, near-surface atmospheric warming drives enhanced surface runoff not only in low-lying ablation zones, but also, though to a smaller degree, in the higher interior accumulation zones (Fig. 2e).

Poleward shift of subtropical highs drives glacier mass loss

Atmospheric warming strongly correlates throughout the air column from the near-surface (T2m) up to the 850 hPa level (T850) (r = 0.85) (Fig. 3c), suggesting a large-scale circulation change origin. Figure 5a shows longterm spatial correlation between T850 derived

from the ERA5 reanalysis[26] and glacier-integrated surface runoff from MAR at 500 m (1940-2023). Strong link is generally found across the South Pacific and Atlantic Oceans, notably nearby the Southern Andes ($r > 0.75$, yellow contour in Fig. 5a). Similar patterns hold for RACMO glacier runoff in the period 1979-2023 (Supplementary Fig. 8c). To explore the drivers of this atmospheric warming, Figure 5b maps longterm trends in T850 ($^\circ$C dec^{-1}; background colour), geopotential height Z850 (m dec^{-1}; grey contours), and wind speed and direction (arrows) derived from ERA5 in 1940-2023. The Southern Pacific Subtropical Gyre, i.e., also called Saint Helena High (SHH in Fig. 5b; 30-45°S/130-160°W) experiences enhanced Z850 (> 2.5 m dec^{-1}), indicating a longterm strengthening. This is supported by stronger anticlockwise atmospheric circulation, and associated synoptic warming through enhanced air subsidence (> 0.2 $^\circ$C dec^{-1}). Superimposed on this, the SHH has undergone a longterm poleward shift since 1940, highlighted by a pronounced southeastward curvature of the geopotential contours (80-110°W). Patagonian glaciers thus experience increased atmospheric pressure (1.01 ± 0.81 m dec^{-1}, $p < 0.05$) (Fig. 5c) that drives enhanced northwesterly warm subtropical air advection, triggering significant atmospheric warming (0.14 ± 0.03 $^\circ$C dec^{-1}, $p < 0.01$), (Fig. 5d) that propagates to the near-surface through air subsidence (0.10 ± 0.03 $^\circ$C dec^{-1}, $p < 0.01$) (Fig. 1d). We conclude that this large-scale atmospheric warming is responsible for the longterm surface runoff increase ($R^2 = 0.90$) (Fig. 5d).

Discussion and conclusion

Carrasco-Escaff et al. (2023)[14] previously explored the SMB response of Patagonian glaciers to climatic controls in the period 1980-2015. Opposite to our results, they found that the interannual variability and trends of glacier SMB were predominantly driven by precipitation ($r = 0.87$), rather than runoff fluctuations ($r = -0.69$). High accumulation years coincide with the formation of an anomalous low pressure system in the Drake Passage (DP in Supplementary Fig. 8b,d), i.e., situated to the south of Cape Horn, in turn favouring stronger westerlies and associated precipitation across Patagonian icefields. We find similar strong correlation between total precipitation and Z850 nearby the Drake Passage in both MAR (1940-2023) and RACMO (1979-2023) (Supplementary Fig. 8b,d). However, our results identify atmospheric warming and subsequent runoff increase as the prime control on SMB fluctuations and trends ($r = -0.80$ in Fig. 3a), while precipitation only plays a secondary role ($r = 0.57$). We attribute this contrast to the fact that our high-resolution data sets i) do not significantly overestimate precipitation across Patagonian Andes compared to gridded observations[21] (Supplementary Fig. 7a), and ii) do not significantly underestimate runoff in low-lying ablation zones[18] (Supplementary Fig. 5c,f). This is further demonstrated by the good agreement between our downscaled mass change estimates from both MAR and RACMO, and recent geodetic, glaciological, and remote sensing records (Fig. 1a and Supplementary Table 2). Climate projections across NPI and SPI under a low (RCP2.6) and a high-end emission scenario (RCP8.5) by 2050[16]

corroborate that the contemporary and future SMB variability and trends currently are, and will remain to be, primarily driven by atmospheric warming and runoff increase.

We ascribe longterm runoff increase to a poleward shift of subtropical high pressure systems, which has been observed in the southern hemisphere in the past four decades with latitudinal displacements ranging from 0.04 to 0.10° per decade[32]. The shift of high pressure gyres result from a positive feedback between anomalous rise in sea surface temperature and change in atmospheric circulation[33]. Subtropical sea surface temperature increase is attributed to anomalous Ekman pumping that strengthens surface convergence, hence transporting more heat from the Equator, and further expanding the tropical warm water zone southward. Oceanic warming in turn affects the atmospheric circulation by enhancing the subtropical high pressure systems, i.e., with stronger anticlockwise wind patterns that reinforce the Ekman pumping[33]. Poleward shift of warm subtropical waters strengthens high pressure gyres while displacing them southward, as reported e.g., for the SHH region in previous studies[33–35]. The drivers of this large-scale ocean-atmosphere interaction remain uncertain but are likely linked to global warming[32], and the SHH poleward shift is thus expected to continue in the future[32]. Here we link the SHH poleward shift, and associated northwesterly warm subtropical air advection, to a longterm surface runoff increase in Patagonia (1940-2023), hence driving enhanced glacier mass loss (Fig. 5d). Climate warming projections predict that mass loss of Patagonian icefields will persist in the future, raising global sea-level by 3.1 mm (RCP2.6) to 3.8 mm (RCP8.5) in the period 2012-2050, further reducing the remaining ice volume by 22% to 27% respectively[16]. Extrapolating our modelled mass loss rates from MAR (26.9 ± 2.4 Gt yr^{-1}) and RACMO (26.2 ± 2.4 Gt yr^{-1}) for the period 1979-2023 (Fig. 1a), and assuming no significant fluctuations in solid ice discharge, we estimate that Patagonian glaciers could completely melt away within the next 200 years.

Methods

SMB and mass change records

For SMB evaluation, we use 74 stake measurements spanning the period 1980-2019, and collected at 38 locations across NPI (2 sites), SPI (26 sites) and CDI (19 sites) (inset maps in Fig. 1a). SMB records were estimated from stakes and firn cores drilled on: i) San Rafael (1984)[36] and Nef (1996)[37] glaciers in NPI; ii) Perito Moreno (1980-1985[38] and 1996-2001[39,40]), De Los Tres (1995-1996)[41], Chico (1994-2001)[42], Cerro Gorra Blanca (1995-2001)[43,44], Tyndall (1998-2000)[45], and Pio XI (2000-2006)[44] glaciers in SPI; and iii) Monte Sarmiento Massif (2013-2019)[6] in CDI. We discarded data compiling less than 3 months of monitoring. For a meaningful comparison, we cumulated downscaled SMB at 500 m from MAR and RACMO over the overlapping months of measurements (Supplementary Fig. 5).

We compare monthly GRACE and GRACE-FO mass change records (and uncertainties)[24] for the period 2002–2022 with input-output method estimates (MB = SMB - D) ([Fig. 1a](#) and [Supplementary Fig. 4](#)). Annual mean D were set to 15.1 $\pm$ 1.1 Gt yr^{-1} in 1968-1999[1] and 24.1$\pm$ 1.7 Gt yr^{-1} in 2000-2023[13], and were equally distributed within each month of the year. Monthly SMB is derived from MAR and RACMO spatially integrated over glacier areas, i.e., ignoring seasonal snow and melt outside glaciers. While this may affect the amplitude of mass change, i.e., with peak snow/melt in winter/summer, it does not affect its trend since snow cannot accumulate outside glacier areas over the years.

Gridded meteorological records

We use two gridded meteorological data sets at 5 km, i.e., CR2MET (1960-2021)[31] and PMET (1980-2020)[30], to evaluate downscaled glacier-integrated total precipitation and snowfall from MAR and RACMO at 500 m spatial resolution ([Supplementary Fig. 7](#)). While the meteorological data sets correlate well in the overlapping period 1980-2020 (R^2 = 0.69), total precipitation is on average 31% (65.5 Gt yr^{-1}) larger in PMET than in CR2MET. Total precipitation in MAR and RACMO show excellent agreement with PMET (R^2 = 0.87 and 0.90; RMSE = 10.6 Gt yr^{-1} and 8.9 Gt yr^{-1} respectively), while being 24% to 26% larger than in CR2MET (54.2 and 55.4 Gt yr^{-1} respectively). We attribute the difference between the two meteorological data sets to the fact that CR2MET may only capture solid precipitation. This is supported by the relatively low RMSE obtained when comparing downscaled snowfall from MAR (13.1 Gt yr^{-1}) and RACMO (12.0 Gt yr^{-1}) to the CR2MET data set, i.e., 8% and 9% of the total precipitation in CR2MET respectively.

We also compare anomalies in annual mean near-surface air temperature (T2m), spatially averaged over glacier areas, from MAR and RACMO with those of CR2MET (1960-2021) and PMET (1980-2020). For a meaningful comparison, anomalies are estimated with respect to the period 1960-1989, or the overlapping period in each data set, i.e., 1979-1989 for RACMO and 1980-1989 for PMET ([Fig. 1c](#)). All four data sets show excellent agreement with 0.74 < R^2 < 0.89, and 0.14°C < RMSE < 0.28°C.

MAR: Modèle Atmosphérique Régional

The Modèle Atmosphérique Régional version 3.14 (MAR3v14) implements the dynamical core developed by Gallée and Schayes (1994)[46] and the physics discussed by Fettweis et al. (2005)[47]. MAR has been used and thoroughly evaluated for glaciated areas including the Greenland ice sheet[48], glaciers and ice caps of the Arctic region[49], and the Antarctic ice sheet[50]. The model incorporates a dedicated Soil Ice Snow Vegetation Atmosphere Transfer (SISVAT) module[51] that is specifically adapted for snow and ice processes[52,53]. Surface melt, percolation and retention in firn, and subsequent surface runoff are simu-

lated in a 30-layer snowpack. Snow albedo is computed in the CROCUS sub-module[54] based on snow grain properties (size, sphericity, dendricity), snow densification, solar zenith angle, cloud optical thickness, and surface meltwater ponding. Here MAR is run at 5 km spatial resolution and forced at its lateral and upper atmospheric boundaries by the latest ERA5 climate reanalysis[26] (1940-2023), within a seven-pixel and one-pixel relaxation zone respectively. Forcing fields include temperature, pressure, specific humidity, wind speed and direction prescribed at the 30 model atmospheric levels. Sea surface temperature is prescribed by ERA5 reanalysis on a 6-hourly basis. Firn is initialised XXXX. Ice albedo is fixed at 0.55 as a constant in space and time. Surface topography and ice mask are derived from the 30" resolution digital elevation model GTOPO30[55] and the XXXX? at 1 km resolution, both down-sampled to 5 km.

Compared to the high-resolution glacier outlines from the Randolph Glacier Inventory version 6 (RGIv6)[56], MAR at 5 km generally overestimates ice extent in low-lying ablation areas, notably in SPI (Supplementary Fig. 1a). Surface topography in glacier areas is overall 609 m lower in MAR than in the high resolution Shuttle Radar Topography Mission (SRTM) digital elevation model (DEM)[29] (Supplementary Fig. 2b), with small outlet glaciers being generally too high, and mountain divides and promontories being too low. As a result, glacier hypsometry, i.e., the area-elevation distribution (Supplementary Fig. 9a), is overestimated at low elevations in MAR (green line) relative to SRTM DEM (black line), notably in ablation areas below 600 m a.s.l., and vice-versa further inland (Supplementary Fig. 9b). Using 74 in situ SMB measurements for model evaluation, we find that MAR overestimates SMB across low-lying outlet glaciers, and underestimates SMB in inland accumulation zones, where erroneous ablation conditions are captured (Supplementary Fig. 5a). Poor agreement with in situ observations (R^2 = 0.05) and large RMSE (6.1 m w.e) indicate that MAR typically underestimate SMB across Patagonian glaciers and icefields. This is supported by an overall mass loss overestimate when comparing MAR-derived mass change (SMB - D) with GRACE/GRACE-FO records (RMSE = 573 Gt) (green and red lines in Supplementary Fig. 4a).

RACMO: Regional Atmospheric Climate Model

The Regional Atmospheric Climate Model version 2.3p2 (RACMO2.3p2) incorporates the dynamical core of the High Resolution Limited Area Model (HIRLAM)[57] and the physics package cycle CY33r1 of the European Centre for Medium-Range Weather Forecasts-Integrated Forecast System (ECMWF-IFS)[58]. The model is specifically adapted to represent surface processes of polar ice sheets and ice caps including the Greenland ice sheet[25], Canadian Arctic[59], Svalbard[60], Iceland[61], Patagonia[18] and Antarctica[62]. The model has a 40-layer snow module simulating melt, percolation and retention into firn and subsequent surface runoff[63]. The model represents dry-snow densification[64], drifting snow erosion[65], and snow albedo based on grain size, cloud optical thickness, solar

zenith angle, and impurity content[66]. RACMO2.3p2 at 5.5 km spatial resolution is forced by ERA5 reanalysis[26] (1979-2023) within a 24-grid-cell-wide relaxation zone at the lateral model boundaries. Forcing consists of temperature, pressure, specific humidity, wind speed and direction being prescribed at the 40 model atmospheric levels every 3 hours. Upper atmospheric relaxation is active[67]. Sea surface temperature is prescribed from the ERA5 reanalysis on a 3-hourly basis. Firn is initialised on 1st January 1979 by prescribing an initial snow depth (4 m), temperature (-10°C) and density profile (300-900 kg m^{-3}), followed by a 5-year spin-up simulation (1979-1983). The spin-up ensures that the snowpack properties reach equilibrium with atmospheric conditions. The presented 1979-2023 simulation is then branched from the 5-year spin-up. Ice albedo is prescribed as a constant field in space and time at 0.55. Surface topography and ice mask are derived from the 30" resolution digital elevation model GTOPO30[55] and the Global Land Cover Characteristics[58] at 1 km resolution, both down-sampled to 5.5 km.

RACMO at 5.5 km spatial resolution resolves the three major icefields relatively well (Supplementary Fig. 1a), but does not capture the smaller neighbouring mountain glaciers outlined in the high-resolution RGIv6 product[56]. Relative to the SRTM DEM[29], RACMO shows patterns of surface elevation bias similar to those of MAR, though being smaller on average (529 m) (Supplementary Fig. 2c). As opposed to MAR, glacier hypsometry in RACMO at 5.5 km is underestimated below 600 m a.s.l. (Supplementary Fig. 9d), as low-lying glaciers are generally not captured. This is supported by model evaluation using 74 in situ measurements (Supplementary Fig. 5d) showing an overall SMB overestimate in the ablation zone. RACMO aligns better with in situ observations ($R^2 = 0.55$) than MAR ($R^2 = 0.05$), although with similar RMSE (6.3 m w.e.) and an over three-fold larger positive bias (3 m w.e.). Comparison to GRACE/GRACE-FO mass loss records confirms a SMB overestimate in RACMO, with an erroneous and persistent mass gain since 2002 (blue line in Supplementary Fig. 4a), in line with previous studies[18,21]. In addition, RACMO-derived mass change RMSE (1161 Gt) is over two-fold larger than that of MAR (573 Gt) (Supplementary Fig. 4a).

Statistical downscaling

MAR (1940-2023) and RACMO (1979-2023) SMB components are statistically downscaled from the native model resolution of 5 km and 5.5 km, respectively, to a 500 m ice mask and topography derived from RGIv6[56] and the high-resolution SRTM DEM[29]. The downscaling procedure corrects individual SMB components for elevation on the 500 m topography, using daily-specific vertical gradients estimated on the native model grids. SMB components (X in Eq. 1) include total precipitation (PR), total sublimation (SU), total melt (ME), and runoff (RU). Drifting snow erosion (ER) is accounted for in RACMO. Vertical gradients are estimated as linear regressions using at least six grid-cells, i.e.,

the current one and five (or more) adjacent pixels. To obtain realistic local estimates, the regression slope (a) is applied to the current grid-cell to compute an intercept (b), i.e., value at sea level. These two regression coefficients are bi-linearly interpolated from the low-resolution model grids onto the high resolution one, and applied to the SRTM DEM surface topography at 500 m (h) as,

$$X_{500\,m} = a_{500\,m} \times h_{500\,m} + b_{500\,m} \tag{1}$$

Melt and runoff are further corrected for surface albedo in regions exposing dark bare ice (albedo < 0.55) in summer, that are unresolved in MAR and RACMO. To that end, we use a 500 m MODIS 16-day product averaged for the period 2000-2023. MODIS bare ice albedo is estimated as the mean of the 5% lowest surface albedo recorded each year, averaged for the period 2000-2023. In addition, daily snowfall fraction (SF_{frac}), i.e., the fraction of snowfall on total precipitation, is statistically downscaled to 500 m following Huai et al. (2022)[68]. Snowfall is thus estimated as,

$$SF_{500\,m} = PR_{500\,m} \times SF_{frac\,500\,m} \tag{2}$$

Rainfall is estimated as a residual as,

$$RA_{500\,m} = PR_{500\,m} - SF_{500\,m} \tag{3}$$

SMB is reconstructed using individual components statistically downscaled to 500 m as,

$$SMB_{500\,m} = PR_{500\,m} - RU_{500\,m} - SU_{500\,m} - ER_{500\,m} \tag{4}$$

Note that the drifting snow erosion flux (ER) is not accounted for in MAR. Refreezing (RF) is estimated as a residual following,

$$RF_{500\,m} = ME_{500\,m} + RA_{500\,m} - RU_{500\,m} \tag{5}$$

Spatial refinement and adjustments

In MAR, statistical downscaling results in a 28% increase in total precipitation (42.8 Gt yr^{-1} for 1940-2023) combined with a 13% increase in surface runoff (26.2 Gt yr^{-1}), in turn enhancing SMB by 38% (18.0 Gt yr^{-1}) (Supplementary Table 1). Total precipitation mostly increases around the hypsometry peak of Patagonian glaciers situated between 1000-1600 m a.s.l. (Supplementary Fig. 9a-c), where MAR at 5 km substantially under-estimates surface elevation and glacier area. This is in excellent agreement with PMET-derived vertical precipitation profile (cyan line in Supplementary Fig. 9c). The same holds for surface runoff, though we find an increase in low-lying regions (0-200 m a.s.l.), where small, dark outlet glaciers were not well captured in the original 5 km product (Supplementary Fig. 9a-c). Compared to in situ SMB records, statistical downscaling significantly

improves upon the native MAR product at 5 km, with higher correlation ($R^2 = 0.84$) and essentially halved RMSE (2.7 m w.e.) (Supplementary Fig. 5a-b). Note that high ablation rates are slightly overestimated in downscaled MAR (Supplementary Fig. 5b), indicating a runoff overestimate. Statistical downscaling however improves MAR-derived mass change agreement with GRACE/GRACE-FO, i.e., the RMSE (358 Gt) is reduced by 38% relative to the native product at 5 km (green lines in Supplementary Fig. 4a-b). To eliminate the remaining negative bias in downscaled MAR mass change, surface runoff is further decreased by 12.5% (28.9 Gt yr^{-1}) across Patagonian glaciers (green line in Supplementary Fig. 4c; Supplementary Table 1). This adjustment reduces mass change RMSE down to 48 Gt compared to GRACE/GRACE-FO (Supplementary Fig. 4c), and decreases SMB RMSE to 2.3 m w.e. relative to in situ measurements (Supplementary Fig. 5c).

In RACMO, runoff increases by 147% (126.2 Gt yr^{-1} for 1979-2023) through statistical downscaling. This is almost balanced by a 69% increase in total precipitation (122.9 Gt yr^{-1}), hence only reducing SMB by 2% (2.1 Gt yr^{-1}) relative to the native product at 5.5 km. RACMO generally underestimates glacier area at all elevations (Supplementary Fig. 9e), notably below and around the Patagonian glacier hypsometry peak (1000-1600 m a.s.l.). Largest increases in total precipitation and runoff are thus found in low-lying (respectively elevated) regions where outlet (respectively mountain) glaciers were not resolved at 5.5 km (Supplementary Fig. 9 e,f). As mentioned in previous studies[18,21], RACMO at 5.5 km exaggerates orographic-forced precipitation across the Andes. This process is amplified through statistical downscaling as demonstrated by large precipitation overestimates relative to the PMET data set (cyan line in Supplementary Fig. 9g). This is supported by large SMB overestimate compared to in situ measurements in the accumulation zone (Supplementary Fig. 5e). Nonetheless, we find that statistical downscaling improves upon the native product at 5.5 km, with higher correlation ($R^2 = 0.80$) and lower RMSE (4.6 m w.e.) (Supplementary Fig. 5d-e). Comparing downscaled RACMO-derived mass change with GRACE/GRACE-FO shows similar positive bias, correlation and RMSE to the native product at 5.5 km (Supplementary Fig. 4d-e), the result of almost unchanged SMB as precipitation increase compensates for enhanced runoff. In line with remote sensing, the amplitude of seasonal mass change has increased, i.e., with higher winter accumulation and summertime ablation. Reducing total precipitation by 32.5% (98.4 Gt yr^{-1} in Supplementary Table 1) across Patagonian glaciers eliminates the remaining positive bias and decreases mass change RMSE to 50 Gt relative to remote sensing (blue line in Supplementary Fig. 4c). This adjustment also improves the vertical profile agreement between the downscaled RACMO and PMET products (cyan line in Supplementary Fig. 9e), and further decreases the SMB RMSE to 4.1 m w.e. compared to in situ records (Supplementary Fig. 5f).

Model uncertainty estimates

Uncertainties in SMB and individual components are estimated as the glacier integrated difference between SMB (components) statistically downscaled to 500 m averaged for the period 1979-2023, including runoff (-12.5%) and total precipitation (-32.5%) adjustments in MAR and RACMO respectively (e.g., Supplementary Fig. 3d-f). These uncertainties are shown in Supplementary Fig. 6 and listed in Supplementary Table 1.

For glacier mass change (MB = SMB - D), we sum the uncertainty in modelled SMB (0.7 Gt yr^{-1}) with that of D estimated at 1.7 Gt yr^{-1} in Minowa et al. (2021)[13]. We thus estimate a model mass change uncertainty of 2.4 Gt yr^{-1} as listed in Supplementary Table 2. For cumulative mass change and contribution to sea-level rise, we sum monthly mass change uncertainty in time (0.2 Gt per month) (Fig. 1a).

References

1. Rignot, E., Rivera, A. & Casassa, G. Contribution of the Patagonia Icefields of South America to Sea Level Rise. *Science* **302**, 434 – 437 (2003).

2. Farinotti, D. *et al.* A consensus estimate for the ice thickness distribution of all glaciers on Earth. *Nature Geoscience* **12**, 168–173 (2019).

3. Millan, R. *et al.* Ice Thickness and Bed Elevation of the Northern and Southern Patagonian Icefields. *Geophysical Research Letters* **46**, 6626–6635 (2019).

4. Rivera, A., Benham, T., Casassa, G., Bamber, J. & Dowdeswell, J. Ice elevation and areal changes of glaciers from the Northern Patagonia Icefield, Chile. *Global and Planetary Change* **59**, 126–137 (2007).

5. Aniya, M. Holocene variations of Ameghino Glacier, southern Patagonia. *The Holocene* **6** (1996).

6. Temme, F. *et al.* Strategies for regional modeling of surface mass balance at the Monte Sarmiento Massif, Tierra del Fuego. *The Cryosphere* **17**, 2343–2365 (2023).

7. Zemp, M. *et al.* Global glacier mass changes and their contributions to sea-level rise from 1961 to 2016. *Nature* **568**, 382–386 (2019).

8. Fürst, J. J. *et al.* The foundations of the Patagonian icefields. *Nature Communications Earth & Environment* **5**, 1 – 10 (2024).

9. Braun, M. H. *et al.* Constraining glacier elevation and mass changes in South America. *Nature Climate Change* **9**, 130–136 (2019).

10. Dussaillant, I. *et al.* Two decades of glacier mass loss along the Andes. *Nature Geoscience* **12**, 802–808 (2019).

11. Hugonnet, R. *et al.* Accelerated global glacier mass loss in the early twenty-first century. *Nature* **592**, 726–731 (2021).

12. Bamber, J. L., Westaway, R. M., Marzeion, B. & Wouters, B. The land ice contribution to sea level during the satellite era. *Environmental Research Letters* **13**, 063008 (2018).

13. Minowa, M., Schaefer, M., Sugiyama, S., Sakakibara, D. & Skvarca, P. Frontal ablation and mass loss of the Patagonian icefields. *Earth and Planetary Science Letters* **561**, 116811 (2021).

14. Carrasco-Escaff, T., Rojas, M., Garreaud, R. D., Bozkurt, D. & Schaefer, M. Climatic control of the surface mass balance of the Patagonian Icefields. *The Cryosphere* **17**, 1127–1149 (2023).

15. Hock, R. *et al.* GlacierMIP – A model intercomparison of global-scale glacier mass-balance models and projections. *Journal of Glaciology* **65**, 453–467 (2019).

16. Bravo, C., Bozkurt, D., Ross, A. N. & Quincey, D. J. Projected increases in surface melt and ice loss for the Northern and Southern Patagonian Icefields. *Nature scientific reports* **11**, 1–13 (2021).

17. Mernild, S. H., Liston, G. E., Hiemstrad, C. & Wilsone, R. The Andes Cordillera. Part III: glacier surface mass balance and contribution to sea level rise (1979–2014). *International journal of Climatology* **37**, 3154–3174 (2017).

18. Lenaerts, J. T. M. *et al.* Extreme precipitation and climate gradients in patagonia revealed by high-resolution regional atmospheric climate modeling. *Journal of Climate* **27**, 4607–4621 (2014).

19. Schaefer, M., Machguth, H., Falvey, M. & Casassa, G. Modeling past and future surface mass balance of the northern patagonia icefield. *Journal of Geophysical Research: Earth Surface* **118**, 571–588 (2013).

20. Schaefer, M., Machguth, H., Falvey, M., Casassa, G. & Rignot, E. Quantifying mass balance processes on the southern patagonia icefield. *The Cryosphere* **9**, 25–35 (2015).

21. Sauter, T. Revisiting extreme precipitation amounts over southern South America and implications for the Patagonian Icefields. *Hydrology and Earth System Sciences* **24**, 2003–2016 (2020).

22. Foresta, L. *et al.* Heterogeneous and rapid ice loss over the Patagonian Ice Fields revealed by CryoSat-2 swath radar altimetry. *Remote Sensing of Environment* **211**, 441–455 (2018).

23. Malz, P. *et al.* Elevation and Mass Changes of the Southern Patagonia Icefield Derived from TanDEM-X and SRTM Data. *Remote Sensing* **10**, 1–17 (2018).

24. Wouters, B., Gardner, A. S. & Moholdt, G. Global glacier mass loss during the GRACE satellite mission (2002-2016). *Frontiers in Earth Science* **7**, 1 – 11 (2019).

25. Noël, B., van de Berg, W. J., Lhermitte, S. & van den Broeke, M. R. Rapid ablation zone expansion amplifies north Greenland mass loss. *Science Advances* **5**, eaaw0123 (2019).

26. Hersbach, H. *et al.* The ERA5 global reanalysis. *Quarterly Journal of the Royal Meteorological Society* **146**, 1999 – 2049 (2020).

27. Noël, B. *et al.* A daily, 1 km resolution data set of downscaled Greenland ice sheet surface mass balance (1958-2015). *The Cryosphere* **10**, 2361 – 2377 (2016).

28. Noël, B. *et al.* Higher Antarctic ice sheet accumulation and surface melt rates revealed at 2 km resolution. *Nature Communications* **14**, 1–11 (2023).

29. Farr, T. G. *et al.* The Shuttle Radar Topography Mission. *Reviews in Geophysics* **45**, 1–33 (2007).

30. Aguayo, R. *et al.* PatagoniaMet: a multi-source hydrometeorological dataset for Western Patagonia. *Scientific data* **11**, 1 – 15 (2024).

31. Boisier, J. P. & Alvarez-Garreton, C. CR2MET: A high-resolution precipitation and temperature dataset for the period 1960-2021 in continental Chile. *Data set Zenodo* **v2.5** (2023). URL https://zenodo.org/records/7529682.

32. Yang, H. *et al.* Poleward Shift of the Major Ocean Gyres Detected in a Warming Climate. *Geophysical Research Letters* **47**, e2019GL085868 (2020).

33. Yang, H., Lu, J., Wang, Q., Shi, X. & Lohmann, G. Decoding the dynamics of poleward shifting climate zones using aqua-planet model simulations. *Climate Dynamics* **58**, 3513–3526 (2022).

34. Roemmich, D. *et al.* Decadal spinup of the South Pacific subtropical gyre. *Journal of Physical Oceanography* **37**, 162–173 (2007).

35. Roemmich, D., Gilson, J., Sutton, P. & Zilberman, N. Multidecadal change of the South Pacific gyre circulation. *Journal of Physical Oceanography* **46**, 1871–1883 (2016).

36. Yamada, T. Glaciological characteristics revealed by 37.6-m deep core drilled at the accumulation area of San Rafael Glacier, the Northern Patagonia Icefield. *Bull. Glacier Res* **4**, 59–67 (1987).

37. Matsuoka, K. & Naruse, R. Mass Balance Features Derived from a Firn Core at Hielo Patagónico Norte, South America. *Arctic, Antarctic, and Alpine Research* **31**, 333–340 (1999).

38. Aristarain, A. J. & Delmas, R. J. Firn-core study from the southern Patagonia ice cap, South America. *Journal of Glaciology* **39** (1993).

39. Rivera, A. *Investigations on Mass Balance and Dynamics of Moreno Glacier based on Field Measurements and Satellite Imagery. Ph.D. dissertation* (Leopold-Franzens-Universitat Innsbruck, 1999).

40. Stuefer, M., Rott, H. & Skvarca, P. Glaciar Perito Moreno, Patagonia: climate sensitivities and glacier characteristics preceding the 2003/04 and 2005/06 damming events. *Journal of Glaciology* **53**, 3–16 (2007).

41. Popovnin, V. V., Danilova, T. A. & Petrakov, D. A. A pioneer mass balance estimate for a Patagonian glacier: Glaciar De los Tres, Argentina. *Global and Planetary Change* **22**, 255–267 (1999).

42. Rivera, A. *Mass balance investigations at Glaciar Chico, Southern Patagonia Icefield, Chile. Ph.D. thesis* (University of Bristol, 2004).

43. Schwikowski, M., Brütsch, S., Saurer, M., Casassa, G. & Rivera, A. First shallow firn core record from Gorra Blanca, Patagonia. *Geophysical Research Abstracts* **5** (2003).

44. Schwikowski, M., Schläppi, M., Santibañez, P., Rivera, A. & Casassa, G. Net accumulation rates derived from ice core stable isotope records of Pío XI glacier, Southern Patagonia Icefield. *The Cryosphere* **7**, 1635–1644 (2013).

45. Shiraiwa, T. *et al.* High net accumulation rates at Campo de Hielo Patagonico Sur, South America, revealed by analysis of a 45.97 m long ice core. *Annals of Glaciology* **35**, 84–90 (2002).

46. Gallée, H. & Schayes, G. Development of a Three-Dimensional Meso-γ Primitive Equation Model: Katabatic Winds Simulation in the Area of Terra Nova Bay, Antarctica. *Monthly Weather Reviews* **122**, 671–685 (1994).

47. Fettweis, X., Gallée, H., Lefebre, F. & van Ypersele, J.-P. Greenland surface mass balance simulated by a regional climate model and comparison with satellite-derived data in 1990–1991. *Climate Dynamics* **24**, 623–640 (2005).

48. Delhasse, A. *et al.* Brief communication: Evaluation of the near-surface climate in ERA5 over the Greenland Ice Sheet. *The Cryosphere* **14**, 957–965 (2020).

49. Maure, D., Kittel, C., Lambin, C., Delhasse, A. & Fettweis, X. Spatially heterogeneous effect of climate warming on the Arctic land ice. *The Cryosphere* **17**, 4645–4659 (2023).

50. Kittel, C. *et al.* Diverging future surface mass balance between the Antarctic ice shelves and grounded ice sheet. *The Cryosphere* **15**, 1215 – 1236 (2021).

51. Ridder, K. D. & Schayes, G. The IAGL Land Surface Model. *Journal of Applied Meteorology and Climatology* **36**, 167–182 (1997).

52. Gallée, H., Guyomarc'h, G. & Brun, E. Impact Of Snow Drift On The Antarctic Ice Sheet Surface Mass Balance: Possible Sensitivity To Snow-Surface Properties. *Boundary-Layer Meteorology* **99**, 1–19 (2001).

53. Lefebre, F., Gallée, H., van Ypersele, J.-P. & Greuell, W. Modeling of snow and ice melt at ETH Camp (West Greenland): A study of surface albedo. *Journal of Geophysical Research Letters Atmospheres* **108**, 4231 (2003).

54. Brun, E., Martin, E., Simon, V., Gendre, C. & Coleou, C. An Energy and Mass Model of Snow Cover Suitable for Operational Avalanche Forecasting. *Journal of Glaciology* **35**, 333–342 (1989).

55. Gesch, D. B., Verdin, K. L. & Greenlee, S. K. New land surface digital elevation model covers the Earth. *Eos, Earth and Space Science News* **80**, 69–70 (1999).

56. RGI Consortium. *Randolph Glacier Inventory–A Dataset of Global Glacier Outlines: Version 6.0: Technical Report* (Global Land Ice Measurements from Space, 2017). URL https://doi.org/10.7265/N5-RGI-60.

57. Undèn, P. *et al. HIRLAM-5: Scientific Documentation* (HIRLAM-5 Project, Norrköping, Sweden, 2002).

58. ECMWF. *IFS Documentation CY33R1, Part IV : PHYSICAL PROCESSES (CY33R1)* (ECMWF, Reading, UK, 2009).

59. Noël, B. *et al.* Six Decades of Glacial Mass Loss in the Canadian Arctic Archipelago. *Journal of Geophysical Research-Earth Surface* **123**, 1430–1449 (2018).

60. Noël, B. *et al.* Low elevation of Svalbard glaciers drives high mass loss variability . *Nature Communications* **11**, 8 (2020).

61. Noël, B. *et al.* North Atlantic Cooling is Slowing Down Mass Loss of Icelandic Glaciers. *Geophysical Research Letters* **49**, e2021GL095697 (2022).

62. van Wessem, J. *et al.* Modelling the climate and surface mass balance of polar ice sheets using RACMO2 – Part 2: Antarctica (1979–2016). *The Cryosphere* **12**, 1479 – 1498 (2018).

63. Ettema, J. *et al.* Climate of the Greenland ice sheet using a high-resolution climate model - Part 1: Evaluation. *The Cryosphere* **4**, 511 – 527 (2010).

64. Ligtenberg, S., Helsen, M. M. & van den Broeke, M. R. An improved semi-empirical model for the densification of Antarctic firn. *The Cryosphere* **5**, 809 – 819 (2011).

65. Lenaerts, J., van den Broeke, M. R., Angelen, J. H., van Meijgaard, E. & Déry, S. J. Drifting snow climate of the Greenland ice sheet: a study with a regional climate model. *The Cryosphere* **6**, 891 – 899 (2012).

66. Kuipers Munneke, P. *et al.* A new albedo parameterization for use in climate models over the Antarctic ice sheet. *Journal of Geophysical Research* **116**, D05114 (2011).

67. van de Berg, W. & Medley, B. Brief Communication: Upper-air relaxation in RACMO2 significantly improves modelled interannual surface mass balance variability in Antarctica . *The Cryosphere* **10**, 459 – 463 (2016).

68. Huai, B., van den Broeke, M., Reijmer, C. & Noël, B. A daily, 1 km resolution Greenland rainfall climatology (1958-2020) from statistical downscaling of a regional atmospheric climate model. *Journal of Geophysical Research Atmospheres* **127**, e2022JD036688 (2022).

Data availability Annual SMB (and components) data sets from MAR3v14 (1940-2023) and RACMO2.3p2 (1979-2023) at 500 m presented in the manuscript will be uploaded on Zenodo upon publication.

Code availability The statistical downscaling technique is presented in Noël et al. (2016, 2023)[27,28].

Authors contribution B. Noël designed the study, prepared the manuscript, conducted the RACMO2.3p2 simulations at 5.5 km, and statistically downscaled the two presented data sets to 500 m. X. Fettweis conducted the MAR3v14 simulations at 5 km. B. Wouters provided mass change records from GRACE/GRACE-FO. S. Lhermitte helped to prepare the MODIS albedo time series. All authors commented on the manuscript.

Competing Interests The authors declare that they have no competing interests.

Correspondence Correspondence and requests for materials should be addressed to Brice Noël. (email: bnoel@uliege.be).
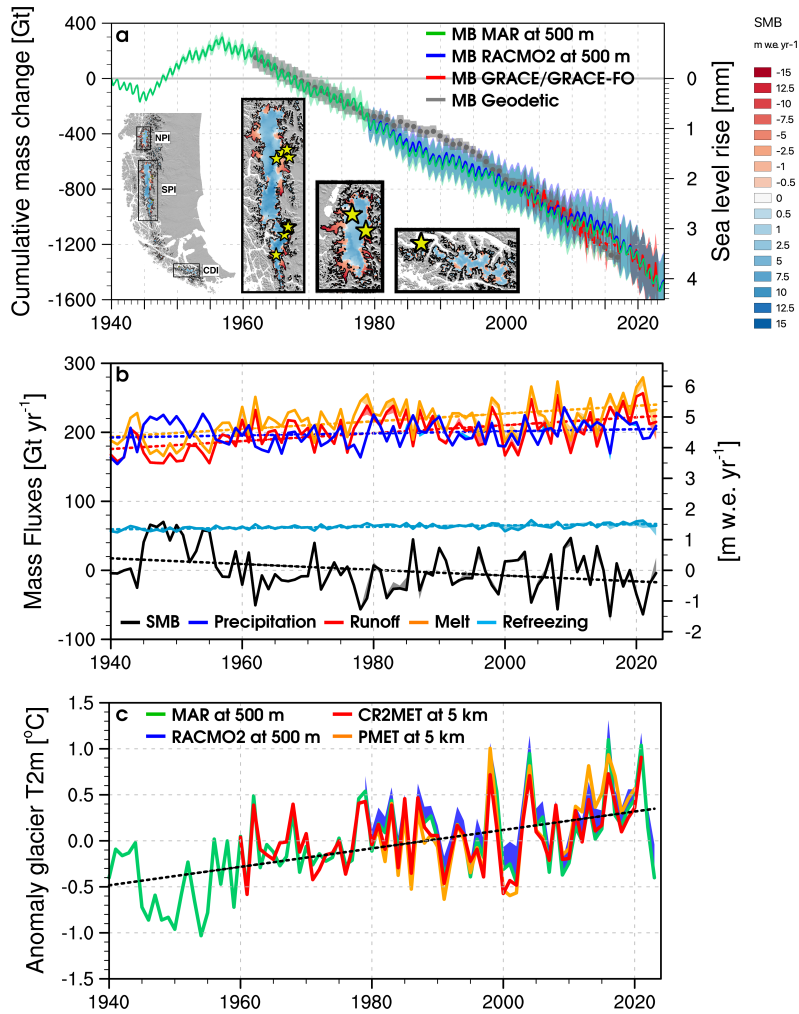
Figure 1: **Longterm mass loss of Patagonian glaciers.** **a** Monthly cumulative mass change (MB = SMB - D) of Patagonian glaciers estimated as the difference between modelled surface mass balance (SMB) from MAR (green line, 1940-2023) and RACMO (blue line, 1979-2023) statistically downscaled to 500 m resolution, and solid ice discharge from Rignot et al. (2003)[1] (1940-1999) and Minowa et al. (2021)[13] (2000-2023). Observed geodetic mass change from Zemp et al. (2019)[7] (1961-2016) and satellite mass change from GRACE/GRACE-FO (2002-2023) are shown in grey and red respectively. Coloured bands represent uncertainties. Inset maps show averaged MAR SMB at 500 m (1940-2023) with a zoom in on three major Patagonian icefields: Northern (NPI) and Southern Patagonian Icefield (SPI), and Cordillera Darwin Icefield (CDI). Mass change is converted to global sea-level rise equivalent assuming that 362 Gt of ice raises sea-level by 1 mm. **b** Annual mean SMB components from MAR (coloured solid lines) and RACMO (coloured bands) at 500 m. **c** Annual mean 2 m air temperature anomaly (relative to 1960-1989), spatially averaged over glacier area from MAR (green line) and RACMO (blue band) at 500 m, from CR2MET (red line, 1960-2021)[31] and PMET (orange band, 1980-2020)[30] meteorological grids at 5 km. In **b-c**, longterm trends are derived from MAR (dashed lines).
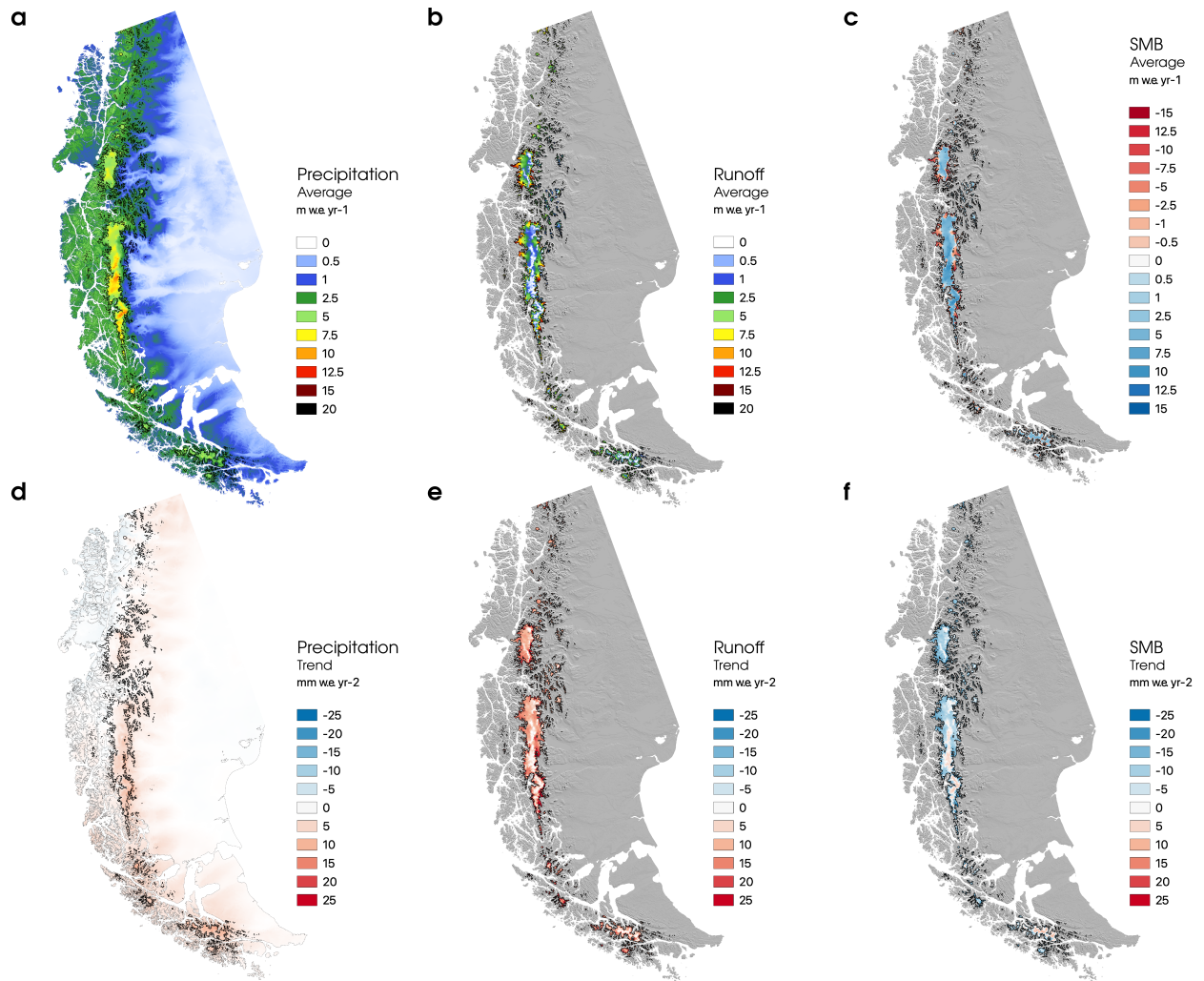
Figure 2: **Longterm SMB components and spatial trends.** Longterm average of **a** total precipitation, **b** adjusted surface runoff and **c** SMB as modelled by MAR, statistically downscaled to 500 m, for the period 1940-2023. **d-f** same as **a-c** but for longterm trends (1940-2023).
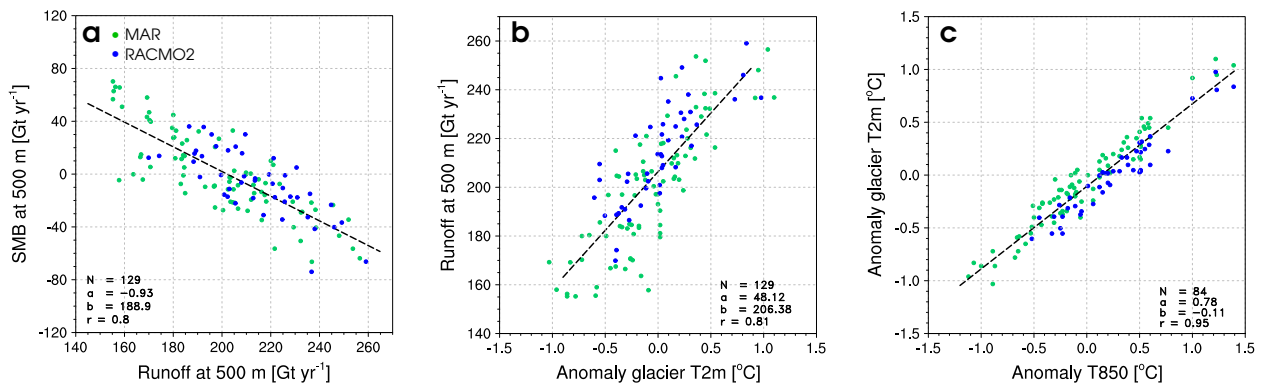
Figure 3: **SMB response to atmospheric temperature anomalies.** Correlation between **a** SMB and surface runoff, **b** surface runoff and anomalies in glacier near-surface temperature (T2m), **c** anomalies in near-surface temperature and anomalies in 850 hPa atmospheric temperature (T850). Anomalies are estimated relative to the 1960-1989 period. MAR and RACMO data at 500 m are shown as blue and green dots respectively. For T2m, model data at 500 m are spatially averaged over glacier areas. Linear regression and relevant statistics, i.e., number of records (N), slope (a), intercept (b), and correlation (r), include both MAR and RACMO data sets. T850 data are extracted from ERA5 reanalysis[26] within the yellow contour shown in Fig. 5a-b.
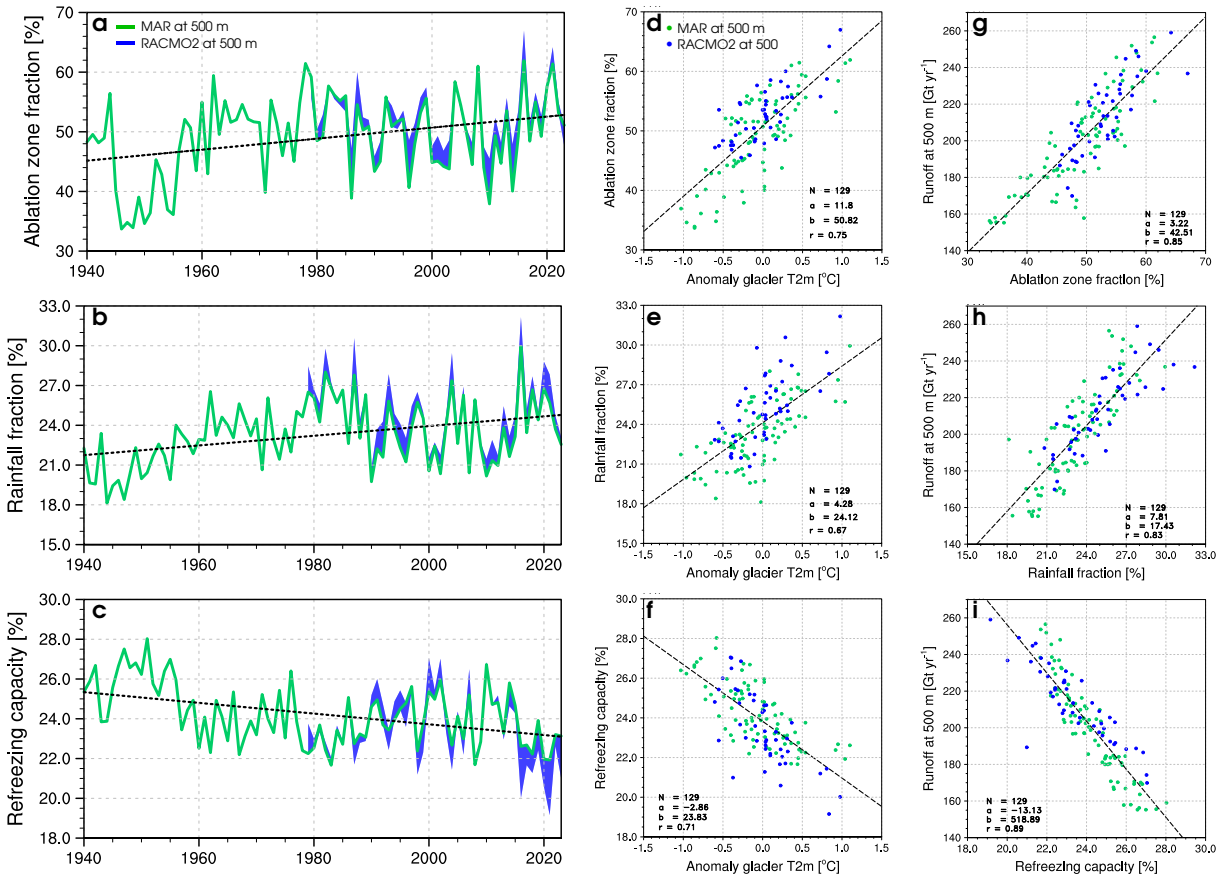
Figure 4: **Longterm trends in SMB processes affecting glacier runoff.** Time series of annual **a** ablation zone fraction (%), i.e., relative to the total glacier area, **b** rainfall fraction (%), i.e., relative to the glacier integrated total precipitation, **c** firn refreezing capacity (%), i.e., the fraction of total melt and rainfall retained or refrozen in firn, for the period 1940-2023. MAR and RACMO data at 500 m are shown as green lines and blue bands, respectively. Longterm trends (1940-2023) derived from MAR are shown as dashed lines. Correlation between anomalies in glacier near surface temperature (T2m, relative to 1960-1989) and **d** ablation zone fraction, **e** rainfall fraction and **f** firn refreezing capacity from MAR (green dots) and RACMO (blue dots) at 500 m. **g-i** same as **d-e** but correlated to surface runoff. In **d-i** linear regression and relevant statistics, i.e., number of records (N), slope (a), intercept (b), and correlation (r), include both MAR and RACMO data sets.
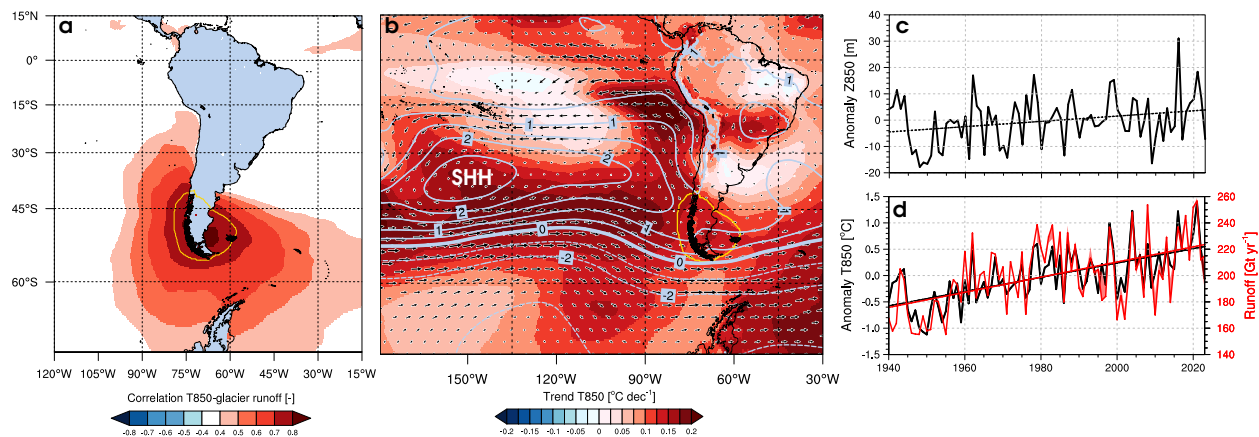
Figure 5: **Poleward shift of subtropical highs enhances surface runoff. a** Spatial correlation between glacier integrated runoff from MAR at 500 m and 850 hPa atmospheric temperature (T850) from ERA5 reanalysis (1940-2023). The yellow contour highlights strong correlation: r > 0.75. **b** Spatial trends in T850 (background map), 850 hPa geopotential height (Z850, m dec^{-1}) (grey contour), and wind direction (arrows). The location of the Saint Helena High (SHH) is also shown. **c** Timeseries of Z850 anomalies relative to 1960-1989, derived from ERA5 reanalysis (1940-2023). **d** Timeseries of T850 anomalies relative to 1960-1989, derived from ERA5 reanalysis (solid black line; 1940-2023); MAR (solid red line; 1940-2023) and RACMO (red band; 1979-2023) runoff timeseries at 500 m are also shown. In **c-d**, Z850 and T850 anomalies are extracted from the region outlined in yellow in **a-b**. Longterm ERA5 (black) and/or MAR (red) trends are shown as dashed lines.

23